GEOPHYSICS®

Probabilistic physics-informed neural network for seismic petrophysical inversion

Journal:	*Geophysics*
Manuscript ID	GEO-2023-0214.R2
Manuscript Type:	Technical Paper
Keywords:	machine learning, inversion, petrophysics, seismic attributes, statistics
Manuscript Focus Area:	Reservoir Geophysics

Probabilistic physics-informed neural network for seismic petrophysical inversion

Peng Li[1], Mingliang Liu[2], Motaz Alfarraj[3,4], Pejman Tahmasebi[5], and Dario Grana[1]

[1] Department of Geology and Geophysics, School of Energy Resources, University of Wyoming, USA

[2] Department of Energy Science and Engineering, Stanford University, USA

[3] Electrical Engineering Department, King Fahd University of Petroleum and Minerals, Saudi Arabia

[4] SDAIA-KFUPM Joint Research Center for Artificial Intelligence, King Fahd University of Petroleum and Minerals, Saudi Arabia

[5] Colorado School of Mines, Golden, CO 80401, USA

DOI:10.1190/geo2023-0214.1

Probabilistic physics-informed neural network for seismic petrophysical inversion

ABSTRACT

The main challenge in the inversion of seismic data to predict the petrophysical properties of hydrocarbon-saturated rocks is that the physical relations that link the data to the model properties are often non-linear and the solution of the inverse problem is generally not unique. As a possible alternative to traditional stochastic optimization methods, we propose to adopt machine learning algorithms by estimating relations between data and unknown variables from a training dataset with limited computational cost. We present a probabilistic approach for seismic petrophysical inversion based on physics-informed neural network with a reparameterization network. The novelty of the proposed approach includes the definition of a physics-informed neural network algorithm in a probabilistic setting, the use of an additional neural network for rock physics model hyperparameters estimation, and the implementation of Approximate Bayesian Computation to quantify the model uncertainty. The reparameterization network allows us to include unknown model parameters, such as rock physics model hyperparameters. The proposed method predicts the most likely model of petrophysical variables based on the input seismic dataset and the training dataset and provides a quantification of the uncertainty of the model. The method is scalable and can be adapted to various geophysical inverse problems. We test the inversion on a North Sea dataset with post-stack and pre-stack data to obtain the prediction of petrophysical properties. Compared to regular neural networks, the predictions of the proposed method show higher accuracy in the predicted results and allow us to quantify the posterior uncertainty.

INTRODUCTION

The expression "seismic petrophysics inversion" generally refers to the prediction of petrophysical properties such as porosity and rock and fluid volumes from seismic data. This method has been implemented in a multitude of approaches, the most common one being a two-step inversion consisting of traditional inversion of seismic data for the estimation of seismic velocities (either acoustic inversion of post-stack data or elastic inversion of pre-stack data) and inversion of seismic velocities for the prediction of petrophysical properties (Doyen, 2007; Azevedo and Soares, 2017; Grana et al., 2021). The inversion generally requires a forward physical model. In reservoir characterization, the seismic forward model is often assumed to be a convolutional one, and the petrophysical forward model is a rock physics model. Alternatively, the inversion can be performed in a single step by combining the forward models (Azevedo and Soares, 2017; Grana et al., 2021).

Due to the uncertainty in the measured data and the physical models, the inverse problem is often ill-posed and the solution is generally non-unique. A common approach is to frame the inverse problem in a probabilistic setting to quantify the uncertainty of the model predictions. Grana et al. (2022) summarize the methods of probabilistic inversion into four classes: Bayesian analytical methods, Monte Carlo methods, stochastic optimization methods, and probabilistic deep learning methods. Generally, analytical algorithms (Buland and Omre, 2003; Grana and Della Rossa, 2010; Grana et al., 2017; Fjeldstad and Grana, 2018) are computationally efficient but they largely require assumptions about the linearization of the forward model or analytical probability distributions of the model variables and data errors. Monte Carlo methods (Mosegaard and Tarantola, 1995; Bosch et al., 2007; Connolly and Hughes, 2016; Sen and Biswas, 2017; Zhu and Gibson, 2018; De Figueiredo et al., 2019a,b; Stuart et al., 2019) allow estimating the unknown posterior distribution of the model variables by sampling from a proposal distribution. Stochastic optimization algorithms such as genetical algorithms, simulating annealing and particle swarm optimizations (Sen and Stoffa, 2013; Aster et al., 2018; Grana et al., 2021) can also be used to estimate the solution of the inverse problem. Monte Carlo methods and stochastic optimization algorithms are generally applied to non-linear inverse problems and/or when the distribution of the model variables is not Gaussian; however, these methods are more computationally expensive than analytical methods. Furthermore, the uncertainty assessment might not be precise if a prior distribution of the model variables is not chosen accurately.

In recent years, machine learning (ML) or deep learning (DL) methods have emerged as a possible alternative (Dramsch, 2020; Bhattacharya, 2021; Bhattacharya and Di, 2022) for automatically mapping relations between measured data and model variables without significant computational cost and prior assumptions. In particular, supervised learning methods allow us to derive the relation between the data and the properties of interest from training data without the use of a physical forward model. Several deep learning algorithms have been adopted in exploration geoscience applications, including fault detection (Hale, 2013; Xiong et al., 2018; Wu et al., 2018), facies classification (Matos et al., 2007; Wrona et al., 2018; Alaudah et al., 2019; Liu et al., 2020), porous media modeling (Kamrava et al., 2020, 2021), seismic inversion (Das et al., 2018; Mosser et al., 2018; Alfarraj and AlRegib, 2019a,b), and petrophysical characterization (Shahraeeni and Curtis, 2011; Shahraeeni et al., 2012; Das and Mukerji, 2020; Verma et al., 2021; Bhattacharya, 2022; Vashisth and Mukerji, 2022). Furthermore, deep learning methods have been combined with probability theory to quantify the model uncertainty (Sengupta et al., 2020; Feng et al., 2021; Yang et al., 2021; Daw et al., 2021; Mosser and Naeini, 2022).

The application of ML and DL algorithms to geophysical applications still has several challenges such as insufficient training data to fit the complex relations between observations and target model variables. For example, in seismic petrophysical inversion, the size of the seismic data (observations) is orders of magnitude larger than the dimension of labeled model variables from well logs measurements (target model variables) due to the high cost of drilling wells, especially in the exploration area. Another challenge is that the training dataset might be biased by the location of the wells which might not account for all possible rock and fluid types. In addition, many deep learning methods do not account for uncertainty quantification due to the high accuracy of the most likely models, however, in geophysical inverse problems data errors and model heterogeneity generally lead to high uncertainty in model predictions.

We propose a probabilistic physics-informed neural network (P-PINN) algorithm for seismic petrophysical inversion with the goal of estimating the most likely model of petrophysical properties, the unknown hyperparameters of the rock physics model, and the uncertainty of the model predictions. Physics-informed neural networks (PINN) method is a subclass of deep learning algorithms that integrate data and physical mathematical models and implement them through neural networks or other kernel-based regression networks (Karniadakis et al., 2021). Unlike the work by Karniadakis et al. (2021), the proposed approach does not adopt partial differential equations, since the physics is based on geophysical models consisting of algebraic equations. Compared to other ML or DL algorithms, PINN algorithms have the advantage of incorporating prior knowledge and/or physical constraints into the networks. PINN algorithms have already been used in geophysical inversion for acoustic impedance inversion (Alfarraj and AlRegib, 2019a) and elastic impedance inversion (Alfarraj and AlRegib, 2019b; Biswas et al., 2019). Furthermore, PINN have been used for solving partial differential equations (PDE) in seismic wave equation (Karimpouli and Tahmasebi, 2020), acoustic wave propagation equation, and full waveform inversion (Rasht-Behesht et al., 2022), as well as joint petrophysical inversion of seismic and resistivity data (Liu et al., 2023). In this work, we formulate PINN in a new probabilistic setting and define a P-PINN for seismic petrophysical inversion and petrophysical uncertainty quantification. The framework of the proposed method includes an inverse network to estimate the relations between seismic data and reservoir model variables, a reparameterization network to estimate the rock physics model hyperparameters in the forward model (e.g., rock physics parameters), and a forward model to integrate the physics models in the network. The novelty of the method also includes the implementation of PINN with an additional neural network for rock physics model hyperparameter estimation of the model and Approximate Bayesian Computation (Beaumont et al., 2002) for uncertainty quantification. The reparameterization network allows for estimating the rock physics model hyperparameters of the rock physics models and quantifying the uncertainty. The proposed P-PINN provides a general framework where the inverse network, the reparameterization network, and the forward model can be modified to adapt to different geophysical models. We apply the method using a North Sea sandstone reservoir dataset, to validate the method in a univariate model setting (e.g., prediction of porosity from post-stack seismic data) and multivariate model setting (e.g., prediction of petrophysical properties from pre-stack seismic data).

THEORY

The general form of the inverse problem aims at predicting the model variables $\boldsymbol{m}$ from measured data $\boldsymbol{d}$ according to the governing physical operator $\boldsymbol{\mathcal{F}}$:

$$\boldsymbol{d} = \boldsymbol{\mathcal{F}}(\boldsymbol{m}) + \boldsymbol{e}, \quad (1)$$

where $\boldsymbol{e}$ represents the measurement errors. In non-linear optimization methods, the goal is to find the value $\hat{\boldsymbol{m}}$ that minimizes the misfit between the measured data $\boldsymbol{d}$ and geophysical model prediction $\hat{\boldsymbol{d}}$:

$$\hat{\boldsymbol{m}} = \mathrm{argmin}_{\boldsymbol{m}}\left(\|\boldsymbol{d} - \hat{\boldsymbol{d}}\,\|\right). \quad (2)$$

In the context of inverse problems, deep learning methods are used to find an approximation of the inverse operator $\boldsymbol{\mathcal{G}} \cong \boldsymbol{\mathcal{F}}^{-1}$ and minimize the difference between the predicted output $\hat{\boldsymbol{m}}$ and the target variables $\boldsymbol{m}$ on a training dataset:

$$\hat{\boldsymbol{m}} = \mathcal{G}(\boldsymbol{d};\boldsymbol{\theta}) \tag{3}$$

where $\boldsymbol{\theta}$ represents the training parameters in the neural networks (i.e., weights and biases).

We propose a new method based on a probabilistic approach to PINN, namely P-PINN for seismic petrophysical inversion that combines the prediction of the most likely model and the estimation of the rock physics model hyperparameters as well as their uncertainty. The architecture includes a physics-informed deep neural network that consists of an inverse network and a forward model, and a reparameterization network (Figure 1). In this setting, $\boldsymbol{d}$ denotes the seismic data, $\boldsymbol{m_L}$ denotes the petrophysical properties from well-log data (labeled data), $\boldsymbol{d_L}$ denotes the corresponding seismic data with respect to $\boldsymbol{m_L}$, $\boldsymbol{\lambda}$ denotes rock physics model hyperparameters, and $\hat{\boldsymbol{d}}$, $\widehat{\boldsymbol{m_L}}$, $\hat{\boldsymbol{\lambda}}$ denote the estimated seismic data, petrophysical properties and rock physics model hyperparameters, respectively.

Physics-informed neural network

To find the optimal estimation of $\mathcal{G} \cong \mathcal{F}^{-1}$, the training parameters $\boldsymbol{\theta}$ are learned either in a supervised or unsupervised manner. In the context of seismic petrophysical inversion, supervised learning requires a training dataset consisting of a set of seismic and petrophysical property pairs [$\boldsymbol{d_L}$, $\boldsymbol{m_L}$]. The learning process is performed by minimizing the petrophysical loss function $L_p(\boldsymbol{\theta})$ between the predicted model variables $\boldsymbol{\hat{m}_L}$ and target (labeled) model variables $\boldsymbol{m_L}$:

$$L_p(\boldsymbol{\theta}) = \sum_{i=1}^{n} C(\boldsymbol{\mathcal{G}}(\boldsymbol{d_L};\boldsymbol{\theta}),\boldsymbol{m_L}) \tag{4}$$

where n represents the number of training samples and C represents the dissimilarity metric, such as the mean squared error (MSE) in a regression problem or cross-entropy in a classification problem.

In the proposed PINN, the physical constraints are embedded in the neural network by adding a seismic loss function $L_s(\boldsymbol{\theta})$ based on the forward model $\boldsymbol{\mathcal{F}}$. Seismic data are the input of the neural network to obtain estimates of the model variables (i.e., $\boldsymbol{\mathcal{G}}(\boldsymbol{d};\boldsymbol{\theta})$), that are then the input of the forward model $\boldsymbol{\mathcal{F}}$ to obtain the predictions of the seismic data (i.e., $\boldsymbol{\mathcal{F}}(\boldsymbol{\mathcal{G}}(\boldsymbol{d};\boldsymbol{\theta}))$). The misfit between the measured and predicted seismic data is then the additional loss term $L_s(\boldsymbol{\theta})$:

$$L_s(\boldsymbol{\theta}) = \sum_{i=1}^{n} C(\boldsymbol{\mathcal{F}}(\boldsymbol{\mathcal{G}}(\boldsymbol{d};\boldsymbol{\theta})),\boldsymbol{d}). \tag{5}$$

The total loss function can then be written as:

$$L_t(\boldsymbol{\theta}) = \alpha L_p(\boldsymbol{\theta}) + \beta L_s(\boldsymbol{\theta}) \tag{6}$$

where α and β are tuning parameters to control the influence of each loss function. The neural network is trained by minimizing the total loss function $L_t(\boldsymbol{\theta})$. After sufficient training, an optimal function $\boldsymbol{\mathcal{G}}$ is built to map measurements $\boldsymbol{d}$ into model variables $\boldsymbol{m}$. The operator $\boldsymbol{\mathcal{G}}$ is used for the model variables predictions $\boldsymbol{m}_p$ when the unseen measurements $\boldsymbol{d}_p$ are given to neural networks.

$$\boldsymbol{m}_p = \boldsymbol{\mathcal{G}}(\boldsymbol{d}_p;\boldsymbol{\theta}). \tag{7}$$

Model hyperparameter estimation

One of the advantages of PINN is that it can provide not only an estimate of the optimal values of the model variables but also an estimate of rock physics model hyperparameters of the forward model. For example, some rock physics parameters $\boldsymbol{\lambda}$ in the forward operator, such as critical porosity and coordination number in granular media models or aspect ratio in inclusion models (Mavko et al., 2020), might be unknown in certain applications. These parameters are often defined based on indirect measurements, core sample images, or nearby field studies. In this work, we estimate the rock physics model hyperparameters from the data simultaneously with the inverse mapping approximation $\boldsymbol{\mathcal{G}}(\boldsymbol{d};\boldsymbol{\theta},\boldsymbol{\lambda})$ within the PINN. Hence, the loss function in Equation (5) is reformulated as:

$$L_s(\boldsymbol{\theta},\boldsymbol{\lambda}) = \sum_{i}^{n} L(\boldsymbol{\mathcal{F}}(\boldsymbol{\mathcal{G}}(\boldsymbol{d};\boldsymbol{\theta},\boldsymbol{\lambda})),\boldsymbol{d}), \tag{8}$$

and the total loss function in Equation (6) can be rewritten as:

$$L_t(\boldsymbol{\theta},\boldsymbol{\lambda}) = \alpha L_p(\boldsymbol{\theta}) + \beta L_s(\boldsymbol{\theta},\boldsymbol{\lambda}). \tag{9}$$

Then the total loss $L_t(\boldsymbol{\theta},\boldsymbol{\lambda})$ is minimized by training the neural network and the model variables predictions are obtained by applying the operator $\boldsymbol{\mathcal{G}}$ with the optimal parameters $\boldsymbol{\lambda}$:

$$\boldsymbol{m_p} = \boldsymbol{\mathcal{G}}(\boldsymbol{d_p};\boldsymbol{\theta},\boldsymbol{\lambda}). \tag{10}$$

Bayesian formulation

To quantify the uncertainty associated with the neural network, a probabilistic approach can be applied by formulating the estimation of the parameters $\boldsymbol{\theta}$ of the neural network $P(\boldsymbol{\theta} \mid \boldsymbol{D})$ given the data $\boldsymbol{D}$ in a Bayesian framework as :

$$P(\boldsymbol{\theta} \mid \boldsymbol{D}) = \frac{P(\boldsymbol{D} \mid \boldsymbol{\theta})P(\boldsymbol{\theta})}{P(\boldsymbol{D})}. \tag{11}$$

When the forward model includes unknown hyperparameters $\boldsymbol{\lambda}$, equation 11 can be rewritten to compute the posterior probability distribution $P(\boldsymbol{\theta},\boldsymbol{\lambda} \mid \boldsymbol{D})$ of the neural parameters $\boldsymbol{\theta}$ and hyperparameters $\boldsymbol{\lambda}$:

$$P(\boldsymbol{\theta},\boldsymbol{\lambda} \mid \boldsymbol{D}) = \frac{P(\boldsymbol{D} \mid \boldsymbol{\theta},\boldsymbol{\lambda})P(\boldsymbol{\theta},\boldsymbol{\lambda})}{P(\boldsymbol{D})} = \frac{P(\boldsymbol{D} \mid \boldsymbol{\theta},\boldsymbol{\lambda})P(\boldsymbol{\theta})P(\boldsymbol{\lambda})}{P(\boldsymbol{D})} \tag{12}$$

where we assume that the neural parameters $\boldsymbol{\theta}$ and hyperparameters $\boldsymbol{\lambda}$ are independent.

We address the estimation of the posterior distribution in equation 12 using the Approximate Bayesian Computation (ABC). ABC is a class of Bayesian statistics methods which approximate the likelihood function with Monte Carlo simulation, and the outcomes of estimations are accepted or rejected according a rejection algorithm (Beaumont et al., 2002; Csilléry et al., 2010; Sunnåker et al., 2013; Fernández et al., 2022). In the proposed approach, at each simulation, the parameters $\boldsymbol{\theta}$ and $\boldsymbol{\lambda}$ are first sampled from the prior distribution, a prediction $\hat{\boldsymbol{D}}$ given $\boldsymbol{\theta}$ and $\boldsymbol{\lambda}$ is then obtained through the neural network model. $\hat{\boldsymbol{D}}$ is accepted if it the acceptance criterion is satisfied:

$$\rho_d(\hat{\boldsymbol{D}},\boldsymbol{D}) \leq \epsilon \tag{13}$$

where ρ_d measures the distance between $\hat{\boldsymbol{D}}$ and $\boldsymbol{D}$ based on a given metric and the threshold ϵ represents a tolerance value. The posterior uncertainty is generally affected by the tolerance value ϵ. By running MC simulations, the posterior distribution is approximated from the accepted models. ABC can be also used for Bayesian model comparison by calculating the posterior ratio of the models and defining a parameter K that assesses the plausibility of two different models M_1 and M_2:

$$K = \frac{P(M_1 \mid \boldsymbol{D})}{P(M_2 \mid \boldsymbol{D})} \tag{14}$$

The posterior ratio K is related to the Bayes factor if the prior models of $P(M_1)$ and $P(M_2)$ are equal.

The ABC method is based on a Monte Carlo simulation that does not require the explicit evaluation of the likelihood function, which is a great advantage especially for the cases where the likelihood model is analytically intractable. The main limitation of the proposed approach is that the posterior uncertainty might depend on the tolerance value. If the tolerance value is too large, the method tends to accept a large number of models (i.e., the prior model is dominant with respect to the data), whereas if the tolerance value is too small, the method tends to accept a small number of models (i.e., the data are dominant with respect to the prior model).

Network architecture

In the context of geophysical inverse problems, the inverse problem aims to estimate the relation between the measured data and the petrophysical model variables, and the forward model aims to embed the seismic and rock physics equation in an unsupervised loss function. The inverse model consists of two deep neural networks: an inverse network (Figure 2a) and a reparameterization network (Figure 2b), for the estimation of petrophysical model variables and of the rock physics model hyperparameters respectively. If the model parameters can be accurately assessed from core measurements, the reparameterization network can be simplified or removed.

The inverse network is extended from the network proposed in Alfarraj and AlRegib (2019a,b) (Figure 2a). The inverse network includes four blocks: Sequential block, Local pattern block, Upscaling block, and Regression block. The Sequential block is designed with three layers of gated recurrent units (GRUs) to capture the low-frequency trend in the input-output relations. The Local pattern block is designed with three 1D convolutional layers followed by a 1D convolutional layer to capture the high-frequency content in the training data. The Upscaling block is designed with two deconvolution layers to balance the resolution mismatch between seismic data (unlabeled) and well (labeled) data. The Regression block is designed with a GRU followed by a fully connected (FC) layer to regress the generated feature from previous layers to the target domain.

In addition to the inverse network, a reparameterization network is also included in the inverse model. The reparameterization network consists of three FC layers (Figure 2b). In the case of seismic petrophysical inversion, the rock physics model hyperparameters are estimated through this neural network and the outputs are passed to the forward model.

APPLICATION

To validate the proposed method, we test the inversion on a dataset from an oil-saturated clastic reservoir in the North Sea. The dataset includes well-log data and 2D simulated maps of porosity, clay volume, and water saturation (Dvorkin et al., 2014). The dataset represents a clastic reservoir with a sequence of oil-saturated sandstone layers alternating with non-reservoir shale layers. A 0°

incident angle seismic dataset and a partially stacked seismic dataset were generated using rock physics relations combined with seismic convolutional models. The goal of the application is to predict reservoir petrophysical properties from seismic data by using the proposed probabilistic PINN method with a limited training dataset. To evaluate the performance of the proposed method, we first test the method for a univariate inverse problem (i.e., porosity) and then extend it to a multivariate setting (i.e., porosity, clay volume, water saturation).

Synthetic example: univariate case

In the first example, porosity is the unknown variable of interest, and we assume that the other variables are known. We create a synthetic seismogram by applying the soft sand model (Dvorkin and Nur, 1996) to calculate the dry-rock elastic moduli, Gassmann's equation to calculate the saturated-rock elastic moduli, and a convolutional model of the 0° incident angle for the reflection coefficients. The wavelet used in the convolutional model is a Ricker wavelet with dominant frequency of 30 Hz. We also add random noise to the seismic data to mimic the measurement errors. The signal-to-noise ratio is 5. The 1D profile at the well location used as a reference model is shown in Figure 3. The reference porosity section and seismic data section (Dvorkin et al., 2014) are shown in Figure 4 and include 337 traces. We randomly extract a subset of 30 traces from both seismic data and porosity model as the input-target pairs of the training dataset and split them into two groups of 24 traces for training and 6 traces for validation, respectively. The target petrophysical properties are converted into the time domain for consistency with seismic data.

We first demonstrate the application of the P-PINN network and compare it to a traditional neural network (NN) without physical constraints. The same training parameters are used for the two training processes with the only difference that a physics-informed loss function is added to the P-PINN network. In the ABC, we adopt the Mean Absolute Error (MAE) between true properties and predicted properties as the threshold for the acceptance / rejection criterion. We then run 500 simulations and the models that satisfy the threshold ($\rho_{d_{por}} < 0.015$) are accepted and the others rejected. In this application, 92 models are accepted with the regular NN and 149 models are accepted using the P-PINN with Bayes factor $K = 1.62$, showing the higher relative plausibility of the P-PINN model. Figure 5 illustrates the comparison of the 1D predictions of the regular NN (Figure 5a) and P-PINN (Figure 5b). The predicted results obtained with the P-PINN show an improvement in terms of prediction accuracy and a smaller uncertainty range. We calculated three metrics, correlation coefficient, the determination coefficient R^2, and the MAE, of the true and estimated properties. The metrics between the true model and the estimated models obtained with the P-PINN and regular NN network are compared in Figure 6.

The inversion is then applied to the 2D section in Figure 4b. The mean and standard deviation of the 2D inversion results for porosity are shown in Figures 7 and 8 respectively. Overall, the P-PINN produces more accurate predictions with a smaller difference between true and predicted porosity (Figure 7). Due to the higher accuracy of the P-PINN, the standard deviation of porosity obtained using P-PINN is smaller (Figure 8). Compared to regular NN, the P-PINN predictions provide better lateral continuity consistent with geological processes, which shows the advantage of incorporating physics models into the neural network.

In this example, we assume that one rock physics model hyperparameter is unknown, namely the coordination number of the rock (i.e., the average number of contacts between mineral grains) and we estimate it using the P-PINN. The true value used in the soft sand model to generate the synthetic seismic dataset is 7 according to the literature values presented for idealized models of a random pack of spherical grains (Dvorkin et al., 2014). The estimated distribution of the coordination number is shown in Figure 9, with a mean equal to 6.91 and a standard deviation as of 0.434. The posterior distributions of the weights of the regular NN and P-PINN are also shown in Figure 10. For simplicity, only the weights of the last regression layer are shown.

Synthetic example: multivariate case

In the second example, we test the proposed method in a multivariate setting, where the model variables of interest are porosity, clay volume, and water saturation. The reference well-log data are shown in Figure 11. We adopt three incident angles (15°, 30°, 45°) to mimic the near, mid, and far angle stacks of the partially stacked seismic dataset. The elastic properties are calculated using the soft sand model with Gassmann's equation and the seismic data are computed by convolving the known source wavelet with the amplitude variation-versus-offset (AVO) approximation of the reflection coefficients (Aki and Richards, 2002). The wavelet is a Ricker wavelet with dominant frequency of 30 Hz. The seismic dataset with random noise is shown in Figure 12, with an average signal-to-noise ratio of 5. The true porosity section and synthetic seismic section are shown in Figure 13 and Figure 14. As in the previous example, 30 traces of input–target properties are extracted as the training dataset with a train-validation ratio of 0.8. In the ABC, we apply the following MAE threshold: $\rho_{d_{por}} < 0.019$ and $\rho_{d_{clay}} < 0.095$ and $\rho_{d_{sat}} < 0.081$, for applying acceptance / rejection. We run 100 simulations and 39 simulations are accepted using regular NN and 69 simulations are accepted using P-PINN with Bayes factor K of 1.77.

Figure 15 illustrates the comparison of 1D predictions of the regular NN (Figure 15a) and P-PINN (Figure 15b) by applying ABC. Overall, the P-PINN provides more accurate results with a smaller difference between true and predicted properties. In particular, the prediction of water saturation is more accurate in the hydrocarbon layers. The comparison of the metrics distributions (correlation and determination coefficients and MAE) between true and accepted models of the three variables are shown in Figure 16 for both regular NN and from P-PINN. Overall, the most likely models from P-PINN have higher correlation coefficient, higher R^2 and lower MAE compared to models obtained with the regular NN. Figures 17 and 18 illustrate the mean and standard deviation of the model variables obtained with NN and P-PINN, respectively. Overall, the P-PINN allows the prediction of both low and high frequency information from the data. The P-PINN results show a smaller standard deviation for all three variables, which indicates lower uncertainty in the prediction results.

In this example, we assume two unknown rock physics hyperparameters, namely the critical porosity and the coordination number and we estimate them using the P-PINN. To generate the reference synthetic seismic data, we used a critical porosity of 0.4 and a coordination number of

7. The estimated distributions of the two rock physics model hyperparameters are shown in Figure 19. The predicted coordination number is 6.92 with a standard deviation of 0.129 and the predicted critical porosity is 0.408 with a standard deviation of 0.0051. The posterior distributions of the network weights are shown in Figure 20 for regular NN and P-PINN. Only the weights from the last regression layer are demonstrated for simplicity.

Additional examples

In this section, we present two additional applications. In the first example, we adopt the model in Figure 13 where we impose the oil-water contact (OWC) at 1.85 s to mimic the presence of oil- and water-saturated rocks within the main reservoir layer. A synthetic seismic dataset is generated with the same forward model used in the previous example (Figure 21). We apply the ABC with the following MAE thresholds: $\rho_{d_{por}} < 0.02\ and\ \rho_{d_{clay}} < 0.11\ and\ \ \rho_{d_{sat}} < 0.05$. We run 100 simulations: 31 simulations are accepted using regular NN and 36 simulations using P-PINN with Bayes factor K of 1.16. The comparison between the inverted properties from regular neural networks and from P-PINN is shown in Figures 22 and 23. Overall, both inversion results are accurate, however the P-PINN method provides lower standard deviations, which means less uncertainty in the predicted results.

In the second example, we invert a real dataset of a 2D seismic section with three partial angle stacks (Figure 24). The real dataset represents a complex clastic reservoir in the North Sea with a sequence of sand and shale layers. The reservoir is partially filled by oil with an irreducible water saturation of approximately 0.12. The average porosity in the reservoir rocks is 0.21 with limited variations in clay content between 0.8 and 0.22. The wavelets for the three angle stacks are extracted from the dataset using a statistical approach. The signal-to-noise ratio varies between 2 and 3. We apply the proposed P-PINN method with two wells which contain petrophysical properties as the training labels. The forward model is as that used in the previous example. In this case, we apply the ABC with MAE thresholds: $\rho_{d_{por}} < 0.033\ and\ \rho_{d_{clay}} < 0.032\ and\ \rho_{d_{sat}} < 0.063$. We run 100 simulations: 21 simulations are accepted using regular NN and 29 simulations using P-PINN with Bayes factor K of 1.38. The inversion results are compared in Figures 25 and 26 in terms of the mean and the standard deviation of the accepted realizations. The inversion results for the regular NN are slightly smoother and with higher standard deviations, whereas the P-PINN better captures some property transitions and estimates a lower uncertainty in the results.

We quantify the performance of the neural network methods using three metrics: correlation coefficient, R^2, and mean absolute error (MAE). The values of these metrics for the univariate case are shown in Table 1 and the values for the multivariate case are in Table 2. Compared to the regular NN, overall improvements for all the model variables obtained by the P-PINN are observed, i.e., higher correlation coefficient and R^2 and lower MAE.

The proposed method is scalable and largely adaptable to different inverse problems by combining the main components of the model, namely the inverse network, reparameterization network, and forward model. For example, the proposed inverse network could be replaced by any other neural network such as convolutional neural network (CNN), recurrent neural network (RNN), Fully connected layers (FC layers), or a combination of them. Similarly, the reparameterization network could be replaced by constant values or spatial functions if the parameters are known or can be estimated from other data and the forward model can be substituted with any physical-mathematical relation. The method can be naturally extended to 3D and time-lapse datasets, but the uncertainty quantification study might be limited by the computational costs of multiple simulations for large datasets.

CONCLUSIONS

We presented a probabilistic approach to physics-informed neural network for seismic petrophysical inversion for the simultaneous estimation of the unknown model variables and the rock physics model hyperparameters. The probabilistic approach adopted for the PINN allows us to quantify the uncertainty in the model variables predictions and parameters estimation. The uncertainty quantification approach is formulated in a Bayesian framework where the posterior distribution of the training parameters (i.e., weights and biases) and the forward model parameters (e.g., rock physics parameters) are assumed to be probability distributions. The posterior distribution is computed using Bayes' rule by sampling the training and forward model parameters from the prior and accepting or rejecting the models using the ABC approach. The novelty of the method is the implementation of an additional neural network for hyperparameter estimation in the PINN network and ABC for uncertainty quantification. The proposed method can be embedded in the network known or partially known physics relations and it is easily scalable. We validated the proposed method with univariate and multivariate models and in both cases, the P-PINN provide more accurate and more precise (i.e., less uncertain) predictions. In both cases, the rock physics model hyperparameters are accurately estimated. The presented examples show the applicability of the methodology and demonstrate the potential of the proposed approach. This method can be applied to various uncertain parameters, such as wavelet dominant frequency, fluid and mineral properties, and reservoir conditions, and it can be applied to multiple reservoir variables including fracture properties, mineral volumes, and partial saturations. The main advantage of the proposed approach is the probabilistic formulation that allows us to quantify the uncertainty in the predictions of the model variables and hyperparameters.

APPENDIX: FORWARD GEOPHYSICAL MODEL

For the rock physics component of the forward geophysical model, we adopt the soft sand (or unconsolidated sand) model (Dvorkin et al., 2014), whereas for the seismic component we adopt the AVO model based on the convolution of a wavelet with Aki-Richards' equations.

The soft sand model first computes the bulk and shear moduli of the dry rock, K_{dry} and μ_{dry}, using Hertz-Mindlin equations and Hashin-Shtrikman modified lower bounds as:

$$K_{HM} = \sqrt[3]{\frac{c^2(1-\phi)^2{\mu_{sol}}^2}{18\pi^2(1-\nu_{sol})^2}P}$$

$$\mu_{HM} = \frac{5-4\nu_{sol}}{5(2-\nu_{sol})}\sqrt[3]{\frac{3c^2(1-\phi)^2{\mu_{sol}}^2}{2\pi^2(1-\nu_{sol})^2}P}$$

$$K_{dry} = \left(\frac{\frac{\phi}{\phi_c}}{K_{HM}+\frac{4}{3}\mu_{HM}} + \frac{1-\frac{\phi}{\phi_c}}{K_{sol}+\frac{4}{3}\mu_{HM}}\right)^{-1} - \frac{4}{3}\mu_{HM}$$

$$\mu_{dry} = \left(\frac{\frac{\phi}{\phi_c}}{\mu_{HM}+\frac{\mu_{HM}}{6}\xi_{HM}} + \frac{1-\frac{\phi}{\phi_c}}{\mu_{sol}+\frac{\mu_{HM}}{6}\xi_{HM}}\right)^{-1} - \frac{\mu_{HM}}{6}\xi_{HM}$$

$$\xi_{HM} = \frac{9K_{sol}+8\mu_{sol}}{K_{sol}+2\mu_{sol}}$$

(A1)

where K_{HM} and μ_{HM} are the Hertz-Mindlin moduli and shear moduli at the critical porosity, ϕ is the porosity, c represents coordinate number, ϕ_c the critical porosity, μ_{sol} the shear moduli of the solid phase, ν_{sol} the Poisson's ratio of solid phase, and P is the effective pressure.

The model combines the dry moduli in equation A1 with Gassmann's equations to compute the bulk and shear moduli of the saturated rock K_{sat} and μ_{sat}:

$$K_{sat} = K_{dry} + \frac{\left(1 - \frac{K_{dry}}{K_{sol}}\right)^2}{\frac{\phi}{K_{fl}} + \frac{(1-\phi)}{K_{sol}} - \frac{K_{dry}}{K_{sol}^2}}$$

$$\mu_{sat} = \mu_{dry}$$

(A2)

where K_{fl} is the bulk modulus of the fluid phase. The P- and S- wave velocity V_p and V_s are then computed as:

$$V_p = \sqrt{\frac{K_{sat} + \frac{4}{3}\mu_{sat}}{\rho}}$$

$$V_s = \sqrt{\frac{\mu_{sat}}{\rho}}$$

(A3)

where $\rho = (1-\phi)\rho_{sol} + \phi\rho_{fl}$ is the density of the saturated rock and is computed using a mass balance of the density of the solid and fluid phases ρ_{sol} and ρ_{fl} weighted by porosity.

We then use the Aki Richards AVO equation to calculate the reflectivity coefficients at each interface time value as a function of the incident angle θ:

$$r_{pp}(\theta) = \frac{1}{2}(1 + \tan^2\theta)\frac{\Delta V_p}{\overline{V_p}} - 4\frac{\overline{V_s}^2}{\overline{V_p}^2}\sin^2\theta\frac{\Delta V_s}{\overline{V_s}} + \frac{1}{2}\left(1 - 4\frac{\overline{V_s}^2}{\overline{V_p}^2}\sin^2\theta\right)\frac{\Delta\rho}{\overline{\rho}}$$

(A4)

where $\overline{V_p}$ is the average P-wave velocity across the interface, $\overline{V_s}$ is the average S-wave velocity across the interface, $\bar{\rho}$ is the average density across the interface, ΔV_p is the P-wave velocity differential across the interface, ΔV_s is the S-wave velocity differential across the interface, and $\Delta\rho$ density differential across the interface.

Finally, the seismic signal $s(\theta)$ for each incident angle θ is computed as a convolution between the wavelet $w(\theta)$ and reflectivity coefficients $r_{pp}(\theta)$:

$$s(\theta) = w(\theta) * r_{pp}(\theta).$$

(A5)

REFERENCES

Aki, K., and P. G. Richards, 2002, Quantitative Seismology, 2nd ed.: University Science Books.

Alaudah, Y., P. Michałowicz, M. Alfarraj, and G. AlRegib, 2019, A machine-learning benchmark for facies classification: Interpretation, **7**, SE175–SE187, doi:10.1190/INT-2018-0249.1.

Alfarraj, M., and G. AlRegib, 2019a, Semi-supervised learning for acoustic impedance inversion: SEG Technical Program Expanded Abstracts, 2298–2302, doi:10.1190/segam2019-3215902.1.

Alfarraj, M., and G. AlRegib, 2019b, Semisupervised sequence modeling for elastic impedance inversion: Interpretation, **7**, SE237–SE249, doi:10.1190/INT-2018-0250.1.

Aster, R. C., B. Borchers, and C. H. Thurber, 2019, Parameter Estimation and Inverse Problems, 3rd ed.: Elsevier. doi:10.1016/B978-0-12-804651-7.00002-X.

Azevedo, L., and A. Soares, 2017, Geostatistical Methods for Reservoir Geophysics: Springer International Publishing. doi:10.1007/978-3-319-53201-1.

Beaumont, M. A., W. Zhang, and D. J. Balding, 2002, Approximate Bayesian computation in population genetics: Genetics, 162(4), 2025-2035.

Bhattacharya, S., 2021, A Primer on Machine Learning in Subsurface Geosciences: Springer International Publishing. doi:10.1007/978-3-030-71768-1.

Bhattacharya, S., 2022, Unsupervised time series clustering, class-based ensemble machine learning, and petrophysical modeling for predicting shear sonic wave slowness in heterogeneous rocks: Geophysics, **87**, D161–D174, doi:10.1190/geo2021-0478.1.

Bhattacharya, S., and H. Di, 2022, Advances in Subsurface Data Analytics: Traditional and Physics-Based Machine Learning: Elsevier Science.

Biswas, R., M. K. Sen, V. Das, and T. Mukerji, 2019, Prestack and poststack inversion using a physics-guided convolutional neural network: Interpretation, **7**, SE161–SE174, doi:10.1190/INT-2018-0236.1.

Bosch, M., L. Cara, J. Rodrigues, A. Navarro, and M. Díaz, 2007, A Monte Carlo approach to the joint estimation of reservoir and elastic parameters from seismic amplitudes: Geophysics, **72**, O29–O39, doi:10.1190/1.2783766.

Connolly, P. A., and M. J. Hughes, 2016, Stochastic inversion by matching to large numbers of pseudo-wells: Geophysics, **81**, M7–M22, doi:10.1190/geo2015-0348.1.

Csilléry, K., M. G. B. Blum, O. E. Gaggiotti, and O. François, 2010, Approximate Bayesian Computation (ABC) in practice: Trends in Ecology and Evolution, **25**, 410–418, doi:10.1016/j.tree.2010.04.001.

Das, V., and T. Mukerji, 2020, Petrophysical properties prediction from prestack seismic data using convolutional neural networks: Geophysics, **85**, N41–N55, doi:10.1190/geo2019-0650.1.

Das, V., A. Pollack, U. Wollner, and T. Mukerji, 2018, Convolutional Neural Network for Seismic Impedance Inversion: SEG Technical Program Expanded Abstracts, **84**, 2071–2075, doi:10.1190/segam2018-2994378.1.

Daw, A., M. Maruf, and A. Karpatne, 2021, PID-GAN: A GAN Framework based on a Physics-informed Discriminator for Uncertainty Quantification with Physics: Proceedings of the 27th ACM SIGKDD Conference on Knowledge Discovery & Data Mining, 237–247, doi:10.1145/3447548.3467449.

Doyen, P., 2007, Seismic Reservoir Characterization: An Earth Modelling Perspective (EET 2): EAGE.

Dramsch, J. S., 2020, 70 Years of Machine Learning in Geoscience in Review: Advances in Geophysics, **61**, 1–55, doi:10.1016/bs.agph.2020.08.002.

Dvorkin, J., and A. Nur, 1996, Elasticity of high-porosity sandstones: Theory for two North Sea data sets: Geophysics, **61**, 1363–1370, doi:10.1190/1.1444059.

Dvorkin, J., M. A. Gutierrez, and D. Grana, 2014, Seismic Reflections of Rock Properties: Cambridge University Press. doi:10.1017/CBO9780511843655.

Feng, R., N. Balling, D. Grana, J.S. Dramsch, and T.M. Hansen, 2021, Bayesian convolutional neural networks for seismic facies classification: IEEE Transactions on Geoscience and Remote Sensing, 59(10), 8933-8940.

Fernández, J., M. Chiachío, J. Chiachío, R. Muñoz, and F. Herrera, 2022, Uncertainty quantification in Neural Networks by Approximate Bayesian Computation: Application to fatigue in composite materials: Engineering Applications of Artificial Intelligence, **107**, 104511, doi:10.1016/j.engappai.2021.104511.

de Figueiredo, L. P., D. Grana, M. Roisenberg, and B. B. Rodrigues, 2019a, Gaussian mixture Markov chain Monte Carlo method for linear seismic inversion: Geophysics, **84**, R463–R476, doi:10.1190/geo2018-0529.1.

de Figueiredo, L. P., D. Grana, M. Roisenberg, and B. B. Rodrigues, 2019b, Multimodal Markov chain Monte Carlo method for nonlinear petrophysical seismic inversion: Geophysics, **84**, M1–M13, doi:10.1190/geo2018-0839.1.

Fjeldstad, T., and D. Grana, 2018, Joint probabilistic petrophysics-seismic inversion based on Gaussian mixture and Markov chain prior models: Geophysics, **83**, R31–R42, doi:10.1190/geo2017-0239.1.

Grana, D., and E. Della Rossa, 2010, Probabilistic petrophysical-properties estimation integrating statistical rock physics with seismic inversion: Geophysics, **75**, O21–O37, doi:10.1190/1.3386676.

Grana, D., T. Fjeldstad, and H. Omre, 2017, Bayesian Gaussian Mixture Linear Inversion for Geophysical Inverse Problems: Mathematical Geosciences, **49**, 493–515, doi:10.1007/s11004-016-9671-9.

Grana, D., T. Mukerji, and P. Doyen, 2021, Seismic Reservoir Modeling: Wiley. doi:10.1002/9781119086215.

Grana, D., L. Azevedo, L. de Figueiredo, P. Connolly, and T. Mukerji, 2022, Probabilistic inversion of seismic data for reservoir petrophysical characterization: Review and examples: Geophysics, **87**, M199–M216, doi:10.1190/geo2021-0776.1.

Hale, D., 2013, Methods to compute fault images, extract fault surfaces, and estimate fault throws from 3D seismic images: Geophysics, **78**, O33–O43, doi:10.1190/geo2012-0331.1.

Kamrava, S., P. Tahmasebi, and M. Sahimi, 2020, Linking Morphology of Porous Media to Their Macroscopic Permeability by Deep Learning: Transport in Porous Media, **131**, 427–448, doi:10.1007/s11242-019-01352-5.

Kamrava, S., P. Tahmasebi, and M. Sahimi, 2021, Physics- and image-based prediction of fluid flow and transport in complex porous membranes and materials by deep learning: Journal of Membrane Science, **622**, 119050, doi:10.1016/j.memsci.2021.119050.

Karimpouli, S., and P. Tahmasebi, 2020, Physics informed machine learning: Seismic wave equation: Geoscience Frontiers, **11**, 1993–2001, doi:10.1016/j.gsf.2020.07.007.

Karniadakis, G. E., I. G. Kevrekidis, L. Lu, P. Perdikaris, S. Wang, and L. Yang, 2021, Physics-informed machine learning: Nature Reviews Physics, **3**, 422–440, doi:10.1038/s42254-021-00314-5.

Liu, M., M. Jervis, W. Li, and P. Nivlet, 2020, Seismic facies classification using supervised convolutional neural networks and semisupervised generative adversarial networks: Geophysics, **85**, O47–O58, doi:10.1190/geo2019-0627.1.

Liu, M., D. Vashisth, D. Grana, and T. Mukerji, 2023, Joint Inversion of Geophysical Data for Geologic Carbon Sequestration Monitoring: A Differentiable Physics-Informed Neural Network Model: Journal of Geophysical Research: Solid Earth, **128**doi:10.1029/2022JB025372.

de Matos, M. C., P. L. Osorio, and P. R. Johann, 2007, Unsupervised seismic facies analysis using wavelet transform and self-organizing maps: Geophysics, **72**, P9–P21, doi:10.1190/1.2392789.

Mavko, G., T. Mukerji, and J. Dvorkin, 2020, The Rock Physics Handbook, 3rd ed.: Cambridge University Press.

Mosegaard, K., and A. Tarantola, 1995, Monte Carlo sampling of solutions to inverse problems: Journal of Geophysical Research: Solid Earth, **100**, 12431–12447, doi:10.1029/94JB03097.

Mosser, L., and E. Z. Naeini, 2022, A comprehensive study of calibration and uncertainty quantification for Bayesian convolutional neural networks — An application to seismic data: Geophysics, **87**, IM157–IM176, doi:10.1190/geo2021-0318.1.

Mosser, L., W. Kimman, J. Dramsch, S. Purves, A. De la Fuente Briceño, and G. Ganssle, 2018, Rapid Seismic Domain Transfer: Seismic Velocity Inversion and Modeling Using Deep Generative Neural Networks: 80th EAGE Conference and Exhibition 2018: Opportunities Presented by the Energy Transitiondoi:10.3997/2214-4609.201800734.

Rasht-Behesht, M., C. Huber, K. Shukla, and G. E. Karniadakis, 2022, Physics-Informed Neural Networks (PINNs) for Wave Propagation and Full Waveform Inversions: Journal of Geophysical Research: Solid Earth, **127**doi:10.1029/2021JB023120.

Sen, M. K., and P. L. Stoffa, 1995, Preface: Advances in Exploration Geophysics, **4**doi:10.1016/S0921-9366(06)80001-0.

Sen, M. K., and P. L. Stoffa, 2013, Global Optimization Methods in Geophysical Invesion: Cambridge University Press.

Sen, M. K., and R. Biswas, 2017, Transdimensional seismic inversion using the reversible jump Hamiltonian Monte Carlo algorithm: Geophysics, **82**, R119–R134, doi:10.1190/GEO2016-0010.1.

Sengupta, U., M. Amos, S. Hosking, C.E. Rasmussen, M. Juniper, and P. Young, 2020, Ensembling geophysical models with Bayesian neural networks: Advances in Neural Information Processing Systems, 33, pp.1205-1217.

Shahraeeni, M. S., and A. Curtis, 2011, Fast probabilistic nonlinear petrophysical inversion: Geophysics, **76**doi:10.1190/1.3540628.

Shahraeeni, M. S., A. Curtis, and G. Chao, 2012, Fast probabilistic petrophysical mapping of reservoirs from 3D seismic data: Geophysics, **77**doi:10.1190/geo2011-0340.1.

Stuart, G. K., S. E. Minkoff, and F. Pereira, 2019, A two-stage Markov chain Monte Carlo method for seismic inversion and uncertainty quantification: Geophysics, **84**, R1003–R1020, doi:10.1190/geo2018-0893.1.

Sunnåker, M., A. G. Busetto, E. Numminen, J. Corander, M. Foll, and C. Dessimoz, 2013, Approximate Bayesian Computation: PLoS Computational Biology, **9**doi:10.1371/journal.pcbi.1002803.

Vashisth, D., and T. Mukerji, 2022, Direct estimation of porosity from seismic data using rock- and wave-physics-informed neural networks: Leading Edge, **41**, 840–846, doi:10.1190/tle41120840.1.

Verma, S., S. Bhattacharya, N. U. M. K. Chowdhury, and M. Tian, 2021, A new workflow for multi-well lithofacies interpretation integrating joint petrophysical inversion, unsupervised, and supervised machine learning: First International Meeting for Applied Geoscience & Energy Expanded Abstracts, 2213–2217, doi:10.1190/segam2021-3584118.1.

Wrona, T., I. Pan, R. L. Gawthorpe, and H. Fossen, 2018, Seismic facies analysis using machine learning: Geophysics, **83**, O83–O95, doi:10.1190/geo2017-0595.1.

Wu, X., L. Liang, Y. Shi, and S. Fomel, 2019, FaultSeg3D: Using synthetic data sets to train an end-to-end convolutional neural network for 3D seismic fault segmentation: Geophysics, **84**, IM35–IM45, doi:10.1190/geo2018-0646.1.

Xiong, W., X. Ji, Y. Ma, Y. Wang, N. M. AlBinHassan, M. N. Ali, and Y. Luo, 2018, Seismic fault detection with convolutional neural network: Geophysics, **83**, O97–O103, doi:10.1190/geo2017-0666.1.

Yang, L., X. Meng, and G. E. Karniadakis, 2021, B-PINNs: Bayesian physics-informed neural networks for forward and inverse PDE problems with noisy data: Journal of Computational Physics, **425**, 109913, doi:10.1016/j.jcp.2020.109913.

Zhu, D., and R. Gibson, 2018, Seismic inversion and uncertainty quantification using transdimensional Markov chain Monte Carlo method: Geophysics, **83**, R321–R334, doi:10.1190/geo2016-0594.1.

		Correlation coefficient	R^2	MAE
Porosity	NN	0.8612	0.7100	0.01411
	P-PINN	0.8717	0.7330	0.01404

Table 1: Comparision of performance metrics between the mean of the predictions from regular NN and from P-PINN of the univariate inverse problem.

		Correlation coefficient	R^2	MAE
Porosity	NN	0.777	0.563	0.018
	P-PINN	0.831	0.666	0.017
Clay volume	NN	0.712	0.432	0.082
	P-PINN	0.755	0.548	0.075
Water saturation	NN	0.840	0.668	0.069
	P-PINN	0.886	0.769	0.062

Table 2: Comparision of performance metrics between the mean of the predictions from regular NN and from P-PINN of the multivariate inverse problem.

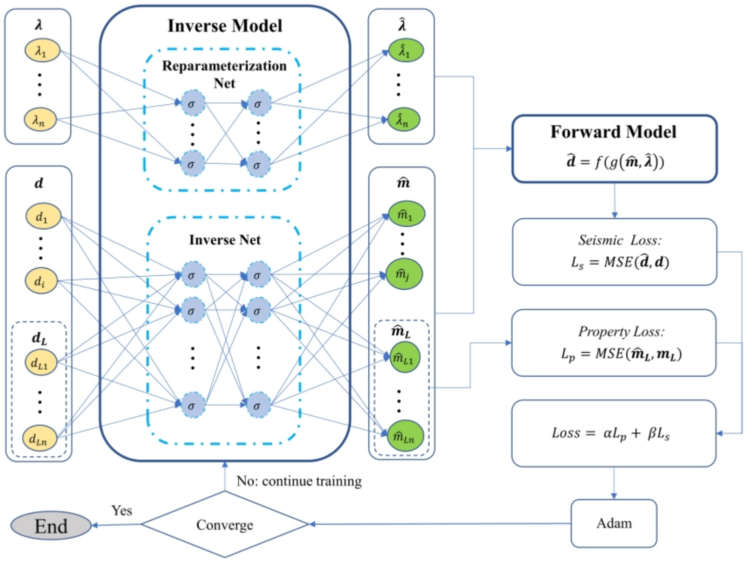

Figure 1: Workflow of the proposed method.

338x190mm (300 x 300 DPI)

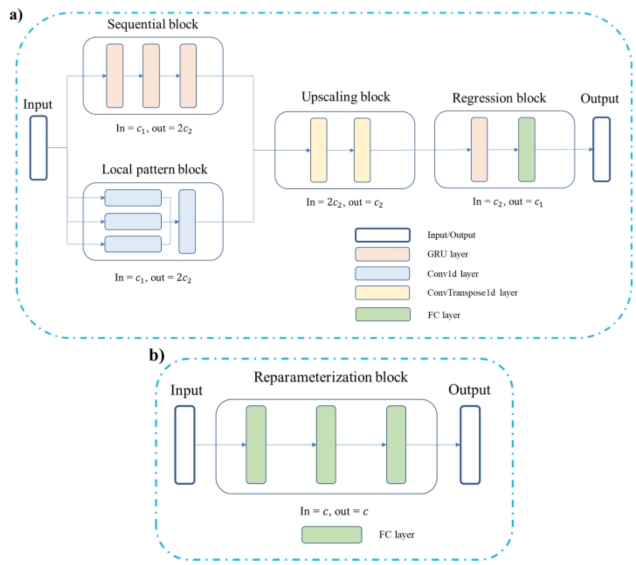

Figure 2: Neural network architectures, a): Inverse net, and b) Reparameterization net.

338x190mm (300 x 300 DPI)

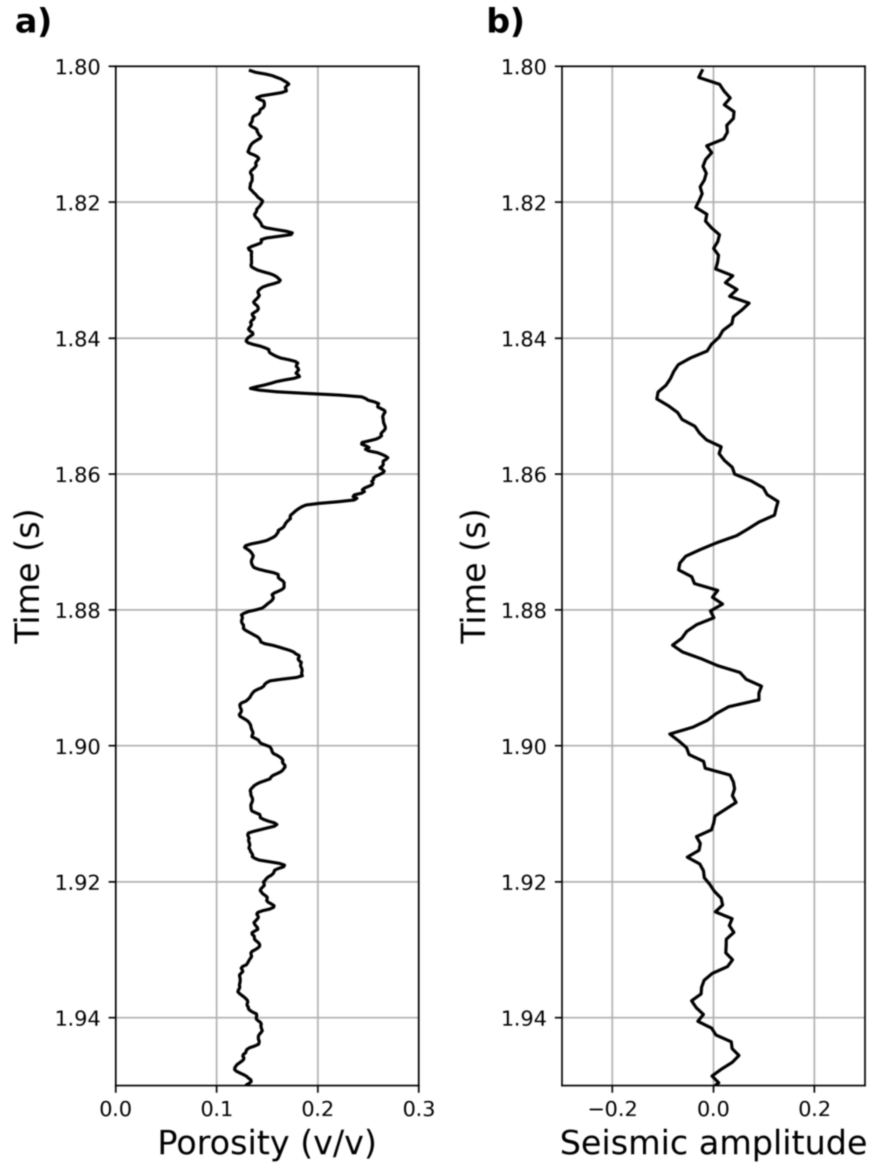

Figure 3: 1D dataset for the univariate inverse problem, a) porosity log, and b) synthetic seismic data.

152x203mm (300 x 300 DPI)

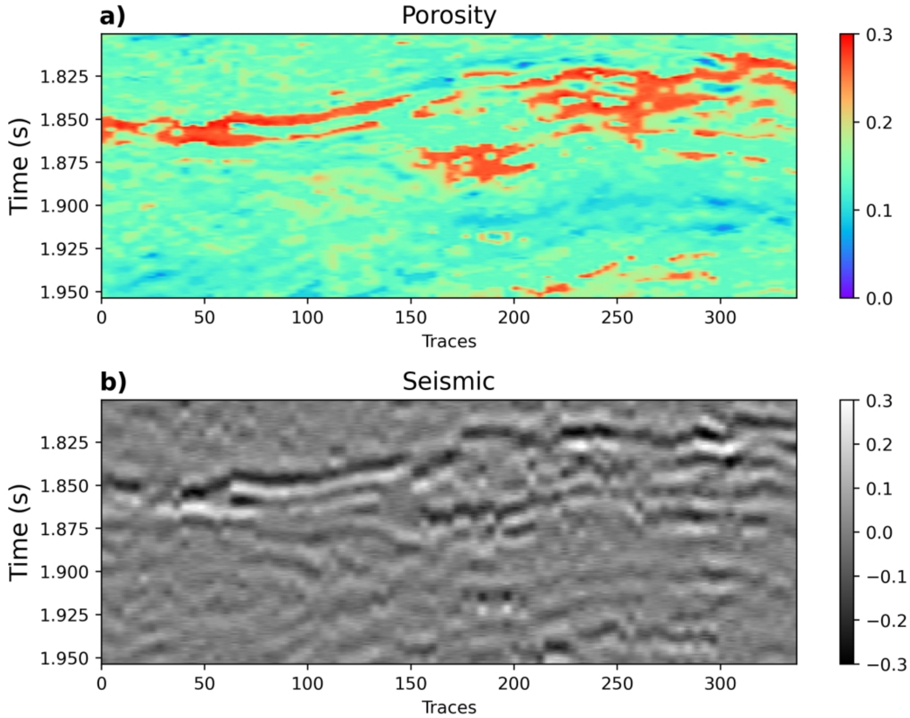

Figure 4: 2D dataset for the univariate inverse problem, a) porosity section, and b) synthetic seismic section.

203x152mm (300 x 300 DPI)

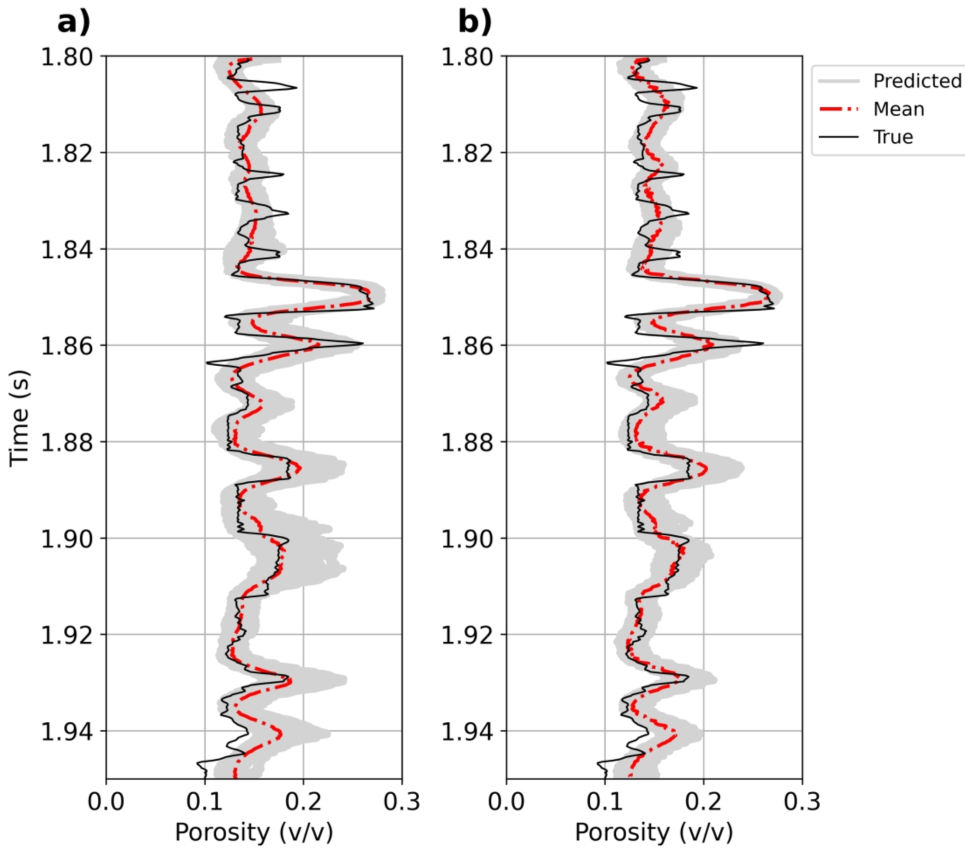

Figure 5: 1D Inversion results for the univariate problem, a) predictions from regular NN, and b) predictions from P-PINN.

203x177mm (300 x 300 DPI)

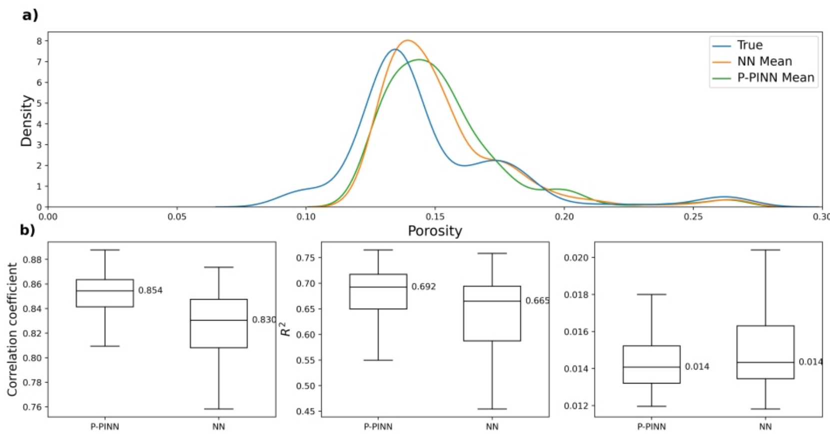

Figure 6: Comparison of metrics distributions (correlation coefficient, R^2, and MAE) between true and estimated models for regular NN and from P-PINN of the univariate inverse problem for one trace.

406x203mm (300 x 300 DPI)

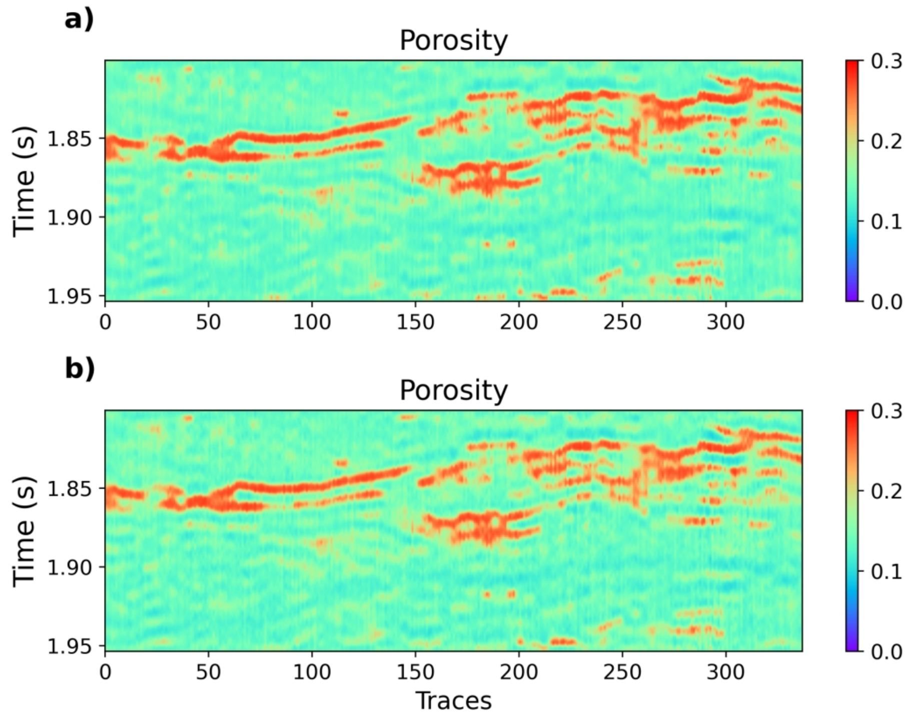

Figure 7: Mean of 2D accepted inversion results of the univariate inverse problem setting, a) predictions from regular NN, and b) predictions from P-PINN.

203x152mm (300 x 300 DPI)

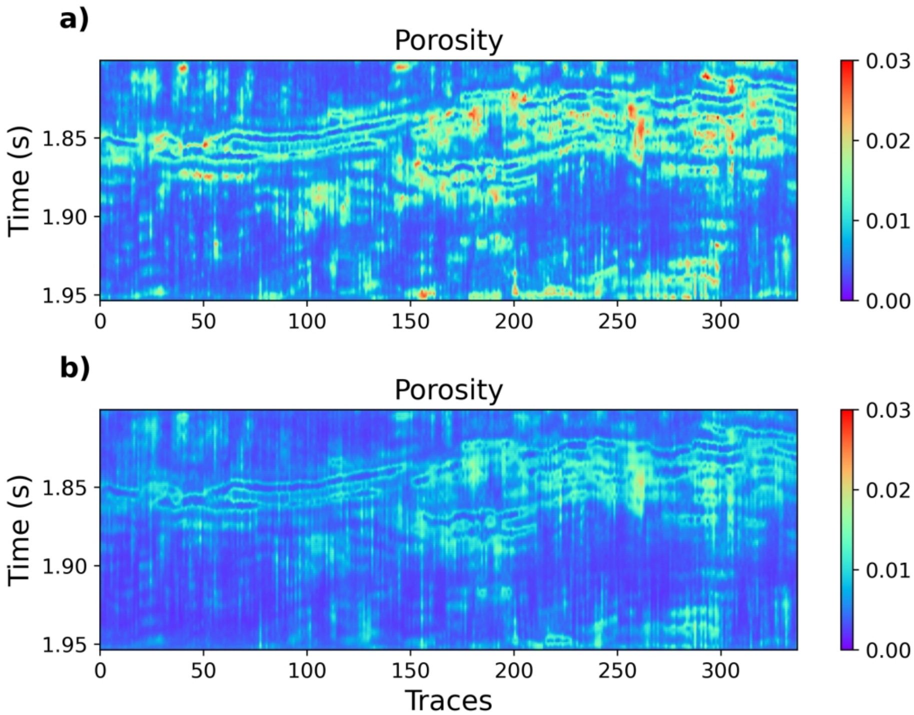

Figure 8: Standard deviation of the accepted inversion results of the univariate inverse problem, a) predictions from regular NN, and b) predictions from P-PINN.

203x152mm (300 x 300 DPI)

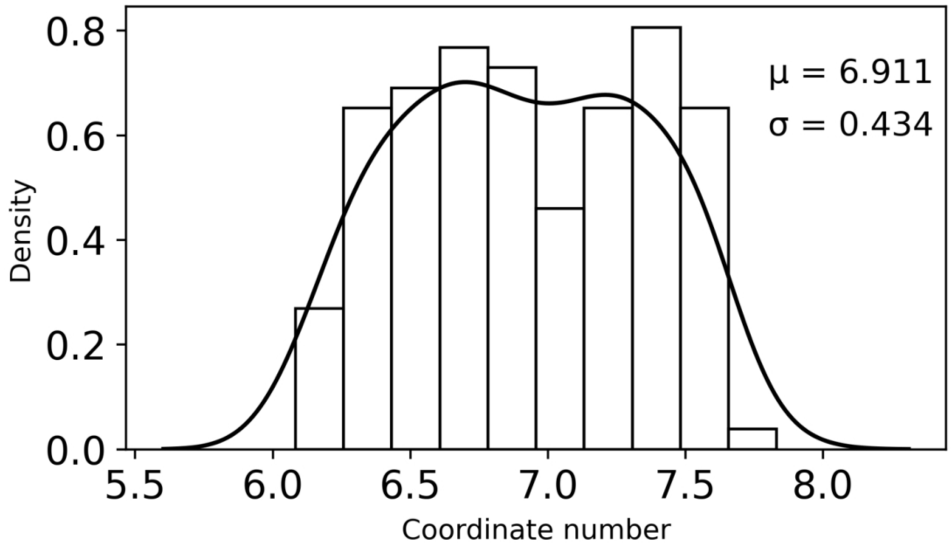

Figure 9: Distribution of estimated rock physics parameter (coordination number) of the univariate inverse problem.

127x76mm (300 x 300 DPI)

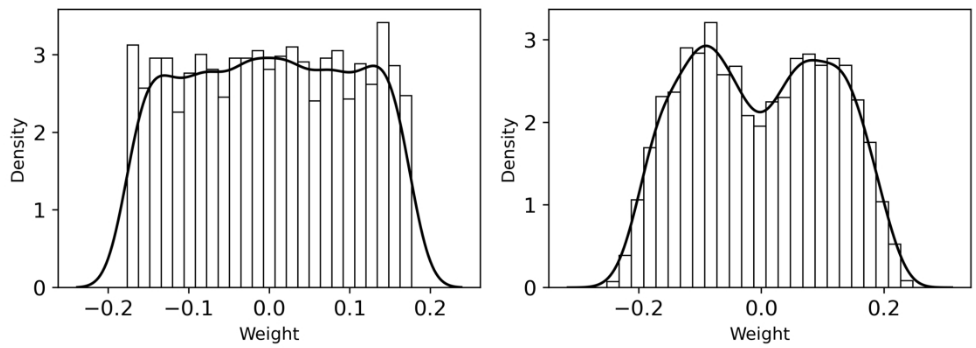

Figure 10: Posterior distributions of weights from the last regression layer: a) weights from regular NN and b) weights from P-PINN

203x76mm (300 x 300 DPI)

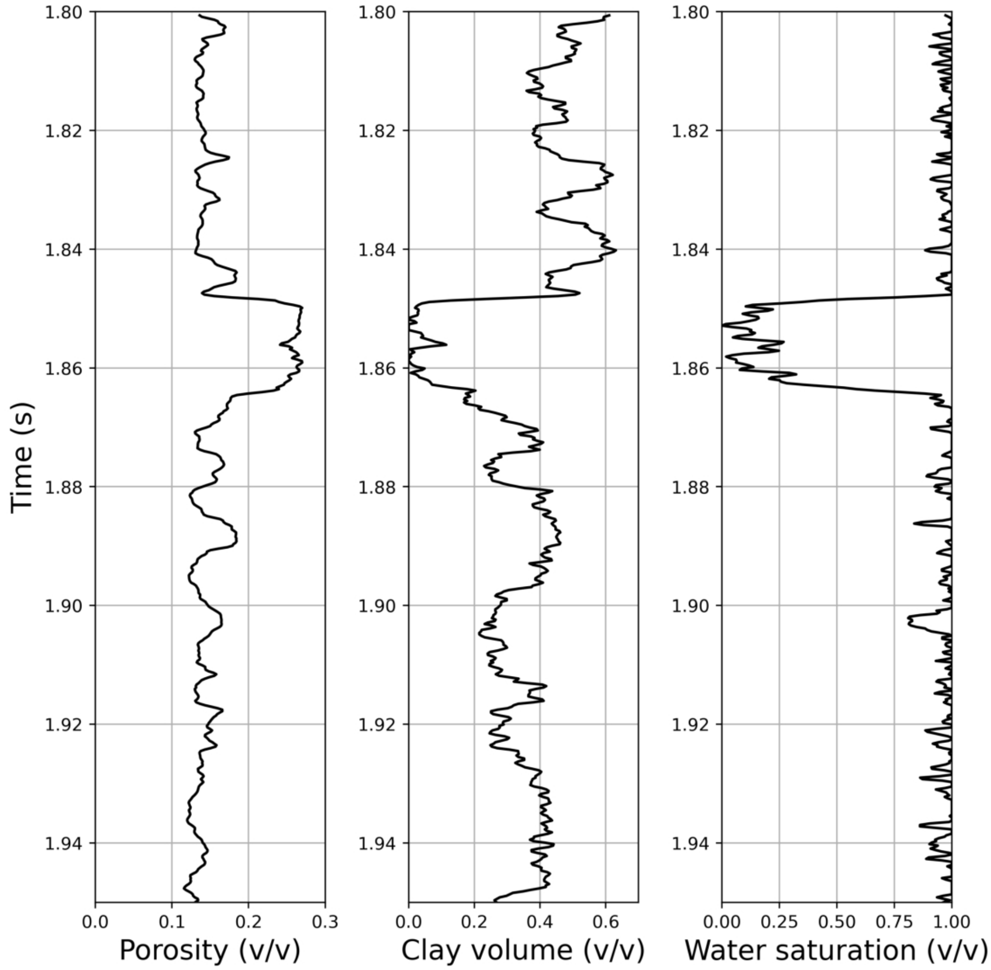

Figure 11: 1D model variables for the multivariate inverse problem, from left to right: porosity, clay volume, and water saturation.

203x203mm (300 x 300 DPI)

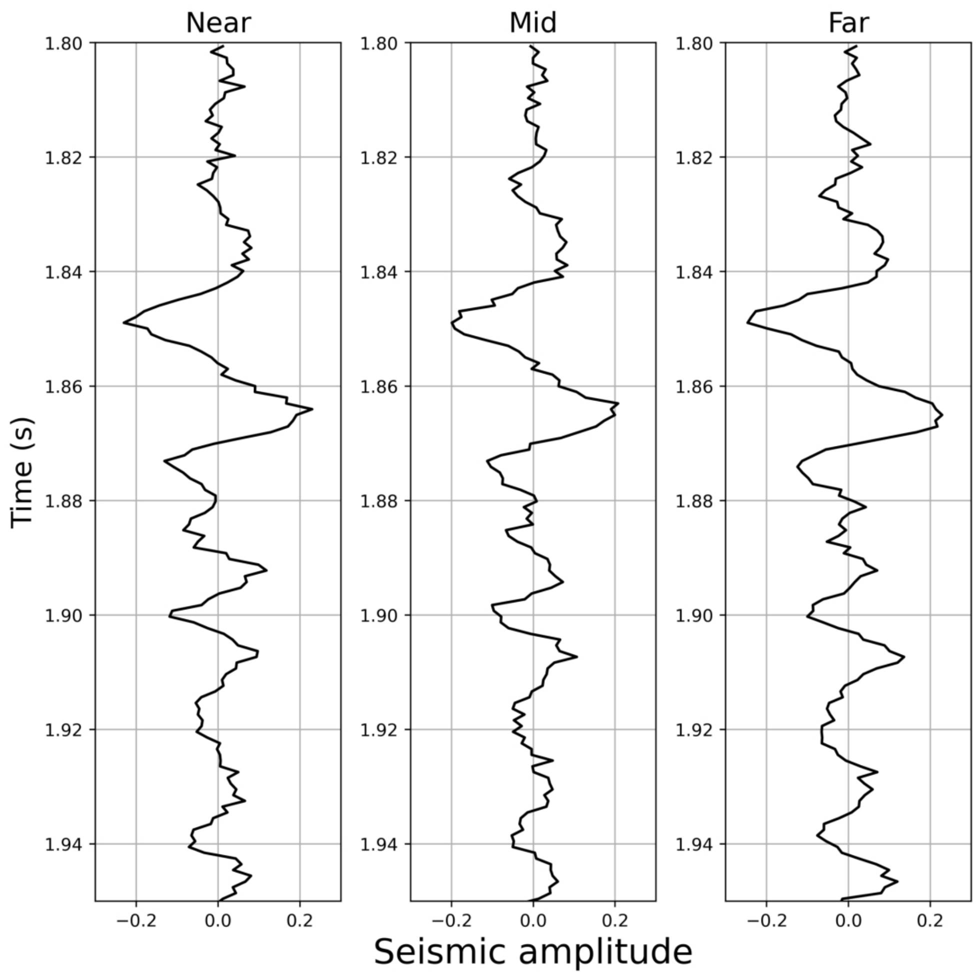

Figure 12: 1D synthetic seismic data with three partial angle stacks of the multivariate inverse problem, from left to right: near (15°), mid (30°) and far (45°).

203x203mm (300 x 300 DPI)

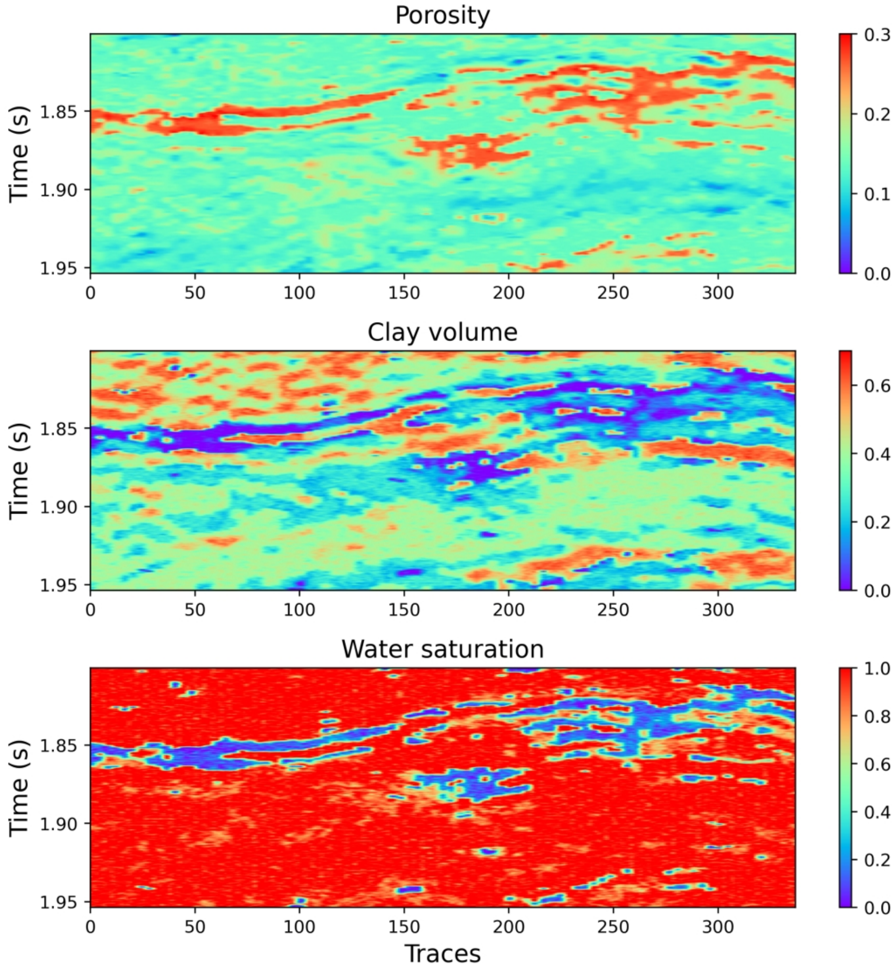

Figure 13: 2D true petrophysical variables of the multivariate inverse problem, from top to bottom: porosity, clay volume, and water saturation.

203x203mm (300 x 300 DPI)

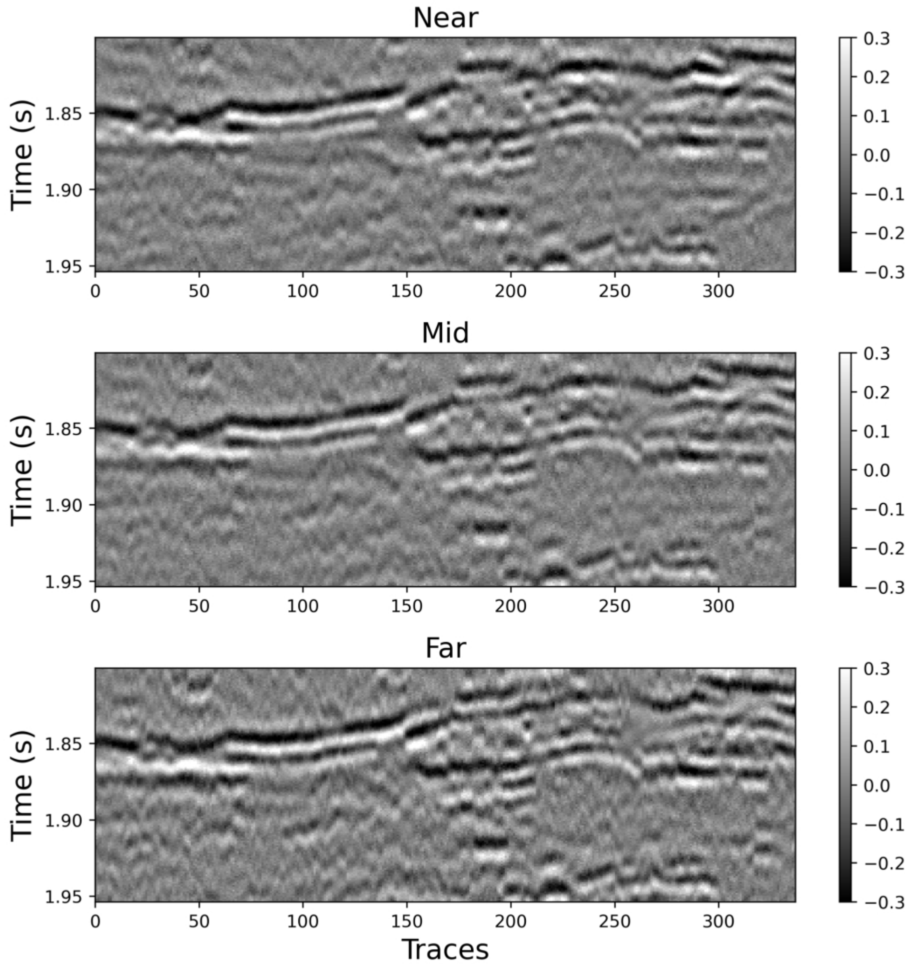

Figure 14: 2D synthetic seismic sections with three partial angles of the multivariate inverse problem, from top to bottom: near (15°), mid (30°) and far (45°).

203x203mm (300 x 300 DPI)

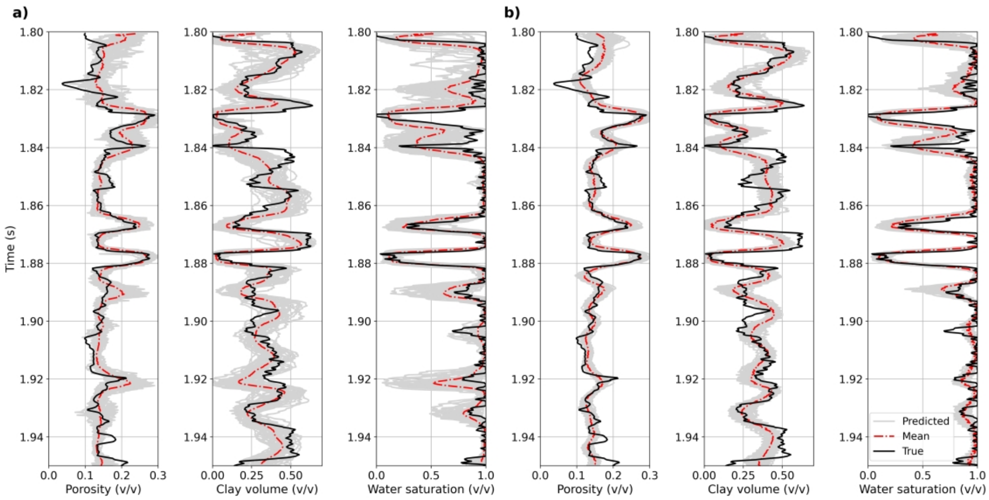

Figure 15: 1D Inversion results of the multivariate inverse problem, a) predictions from regular NN, and b) predictions from P-PINN.

487x244mm (300 x 300 DPI)

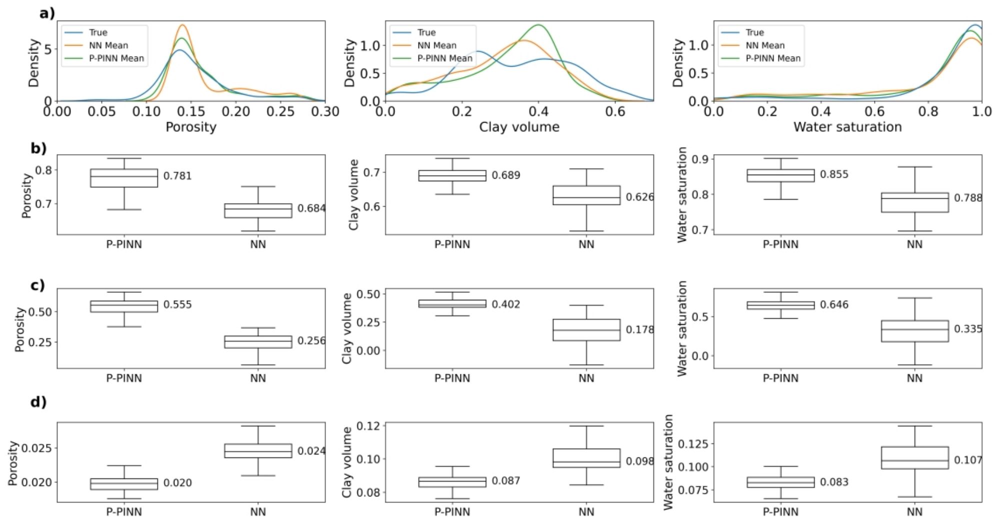

Figure 16: Comparison of metrics distributions (from top to bottom: a) Correlation coefficient, b) R^2, and c) MAE) between true and estimated models for regular NN and from P-PINN of the multivariate inverse problem for one trace.

488x257mm (300 x 300 DPI)

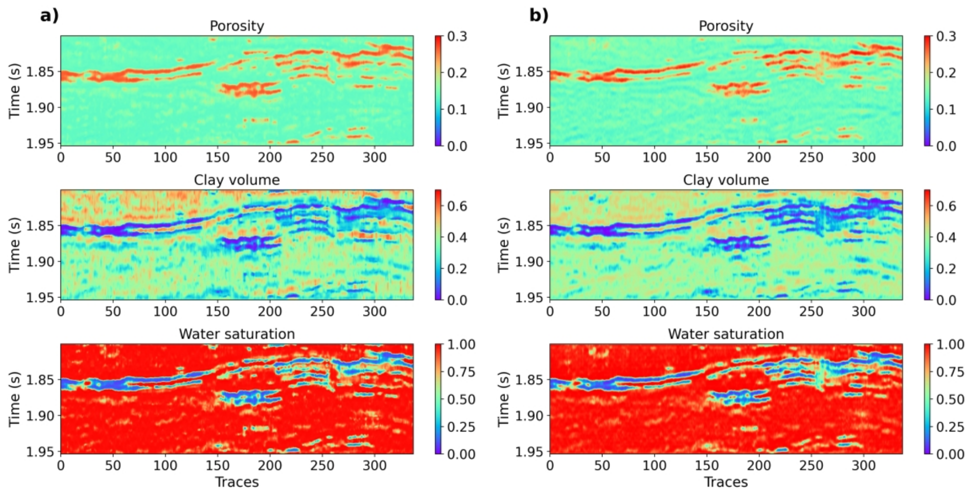

Figure 17: Mean of 2D accepted inversion results of the multivariate inverse problem, a) predictions from regular NN, and b) predictions from P-PINN.

406x203mm (300 x 300 DPI)

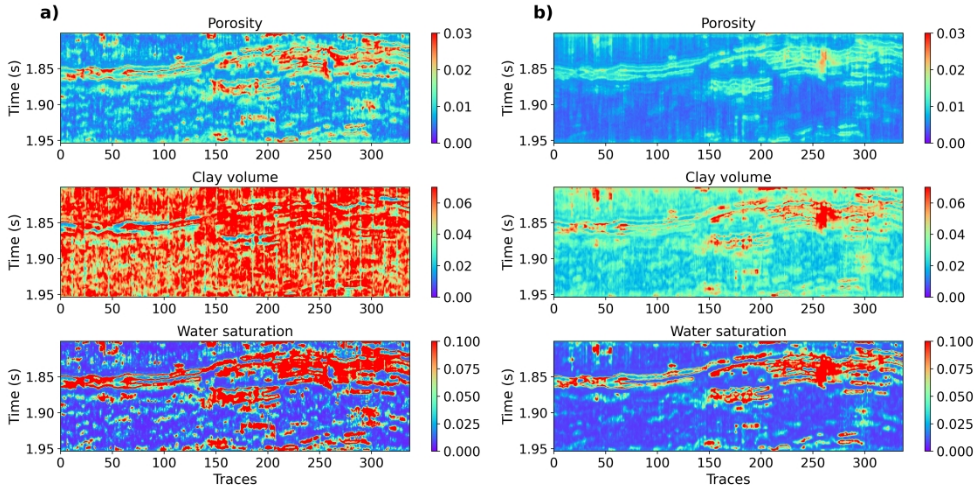

Figure 18: Standard deviation of the accepted inversion results of the multivariate inverse problem, a) predictions from regular NN, and b) predictions from P-PINN.

406x203mm (300 x 300 DPI)

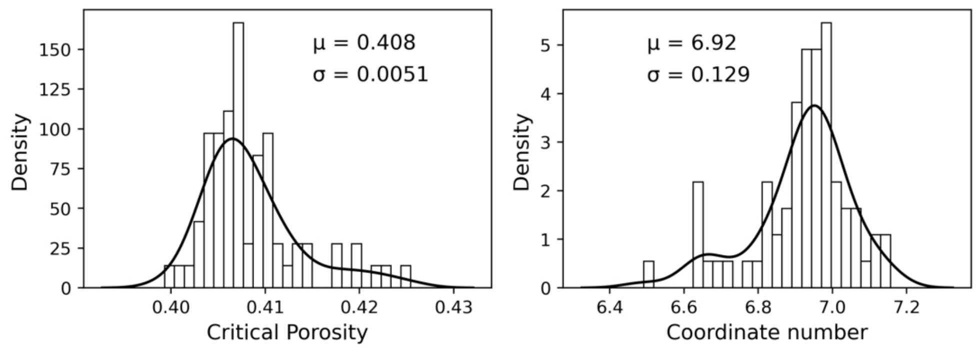

Figure 19: Distributions of estimated unknown rock physics hyperparameters of the multivariate inverse problem: a) estimated critical porosity, and b) estimated coordination number.

203x76mm (300 x 300 DPI)

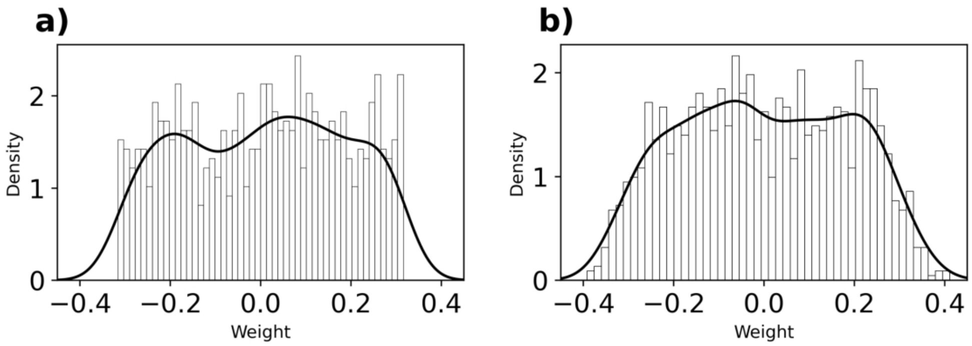

Figure 20: Posterior distributions of weights from the last regression layer: a) weights from regular NN and b) weights from P-PINN.

203x76mm (300 x 300 DPI)

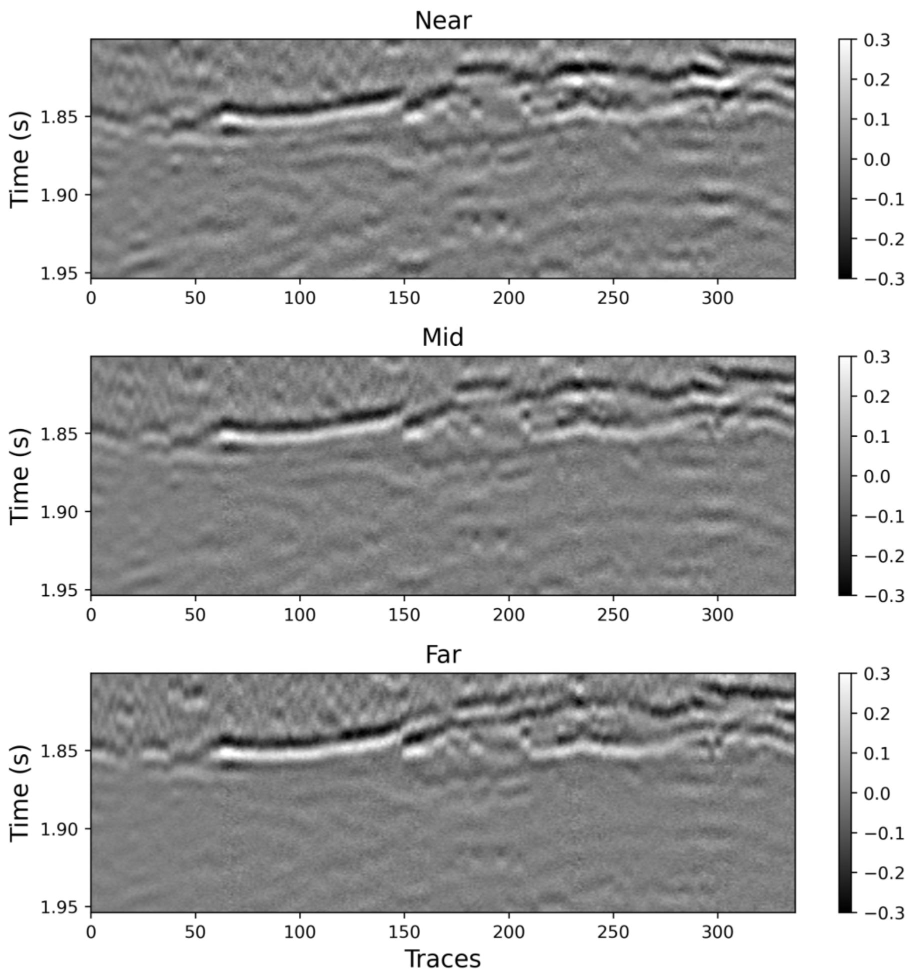

Figure 21: Synthetic seismic data with oil-water contact (OWC) at 1.85s.

203x203mm (300 x 300 DPI)

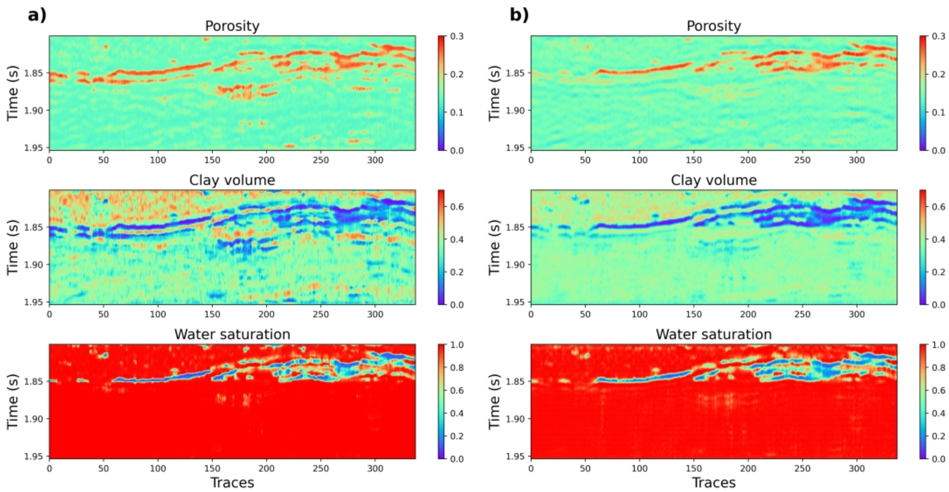

Figure 22: Inversion results for the synthetic case with OWC at 1.85s: a) means from regular NN, and b) means from P-PINN.

406x203mm (300 x 300 DPI)

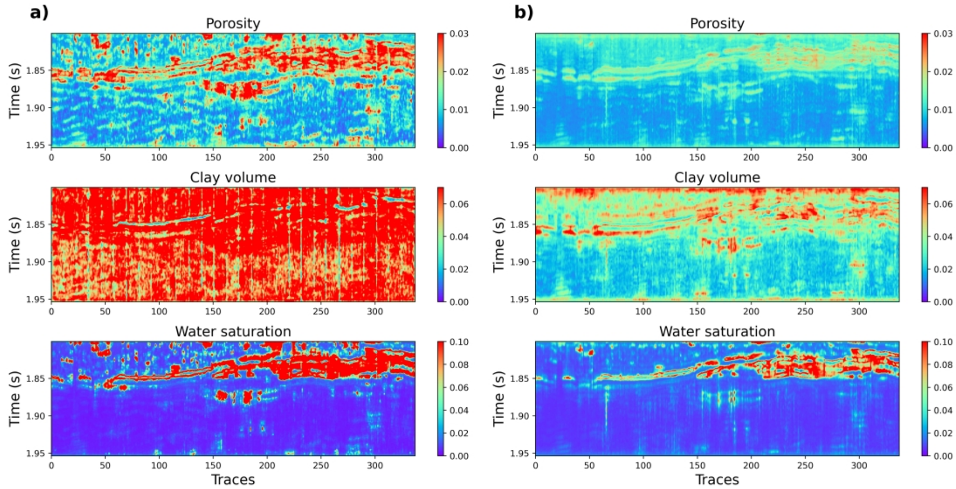

Figure 23: Uncertainty of inversion results for the synthetic case with OWC at 1.85s: a) standard deviations from regular NN, and b) standard deviations from P-PINN.

406x203mm (300 x 300 DPI)

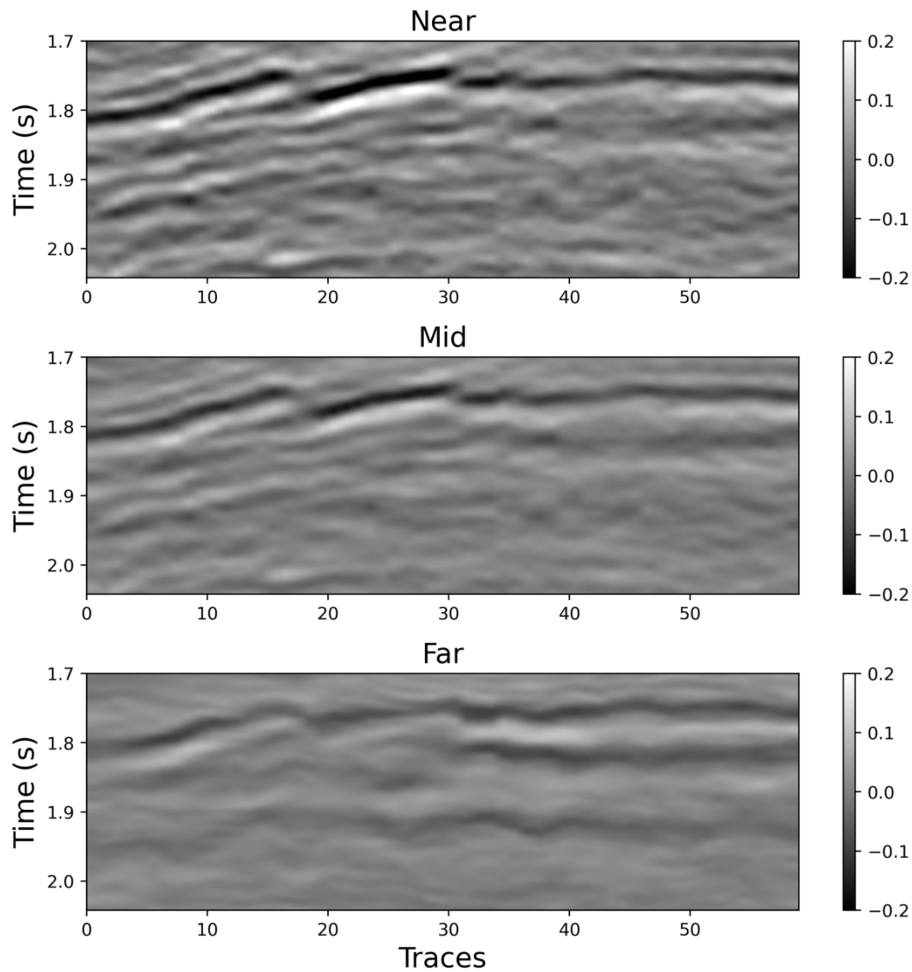

Figure 24: Seismic data for the real case application. The dataset includes three partial angle stacks: Near (15°), Mid (30°) and Far (45°)

203x203mm (300 x 300 DPI)

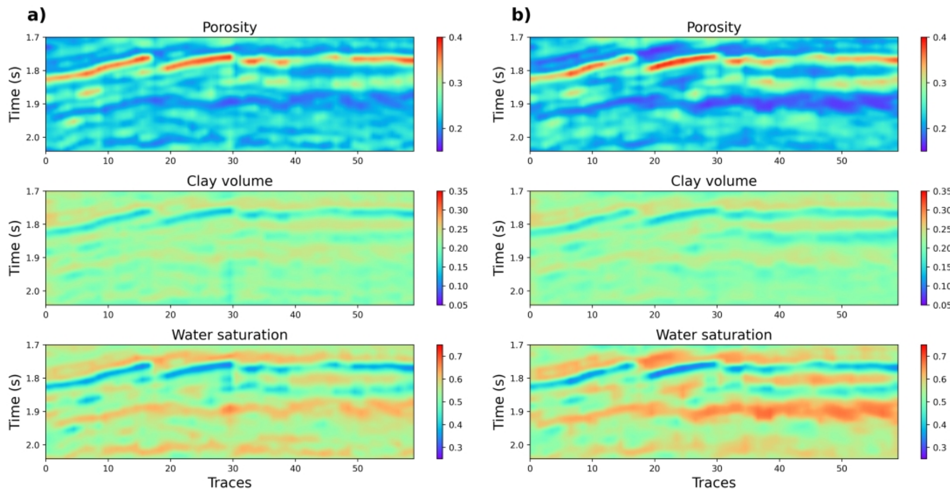

Figure 25: Inversion results for the real case application: a) means from regular NN, and b) means from P-PINN.

406x203mm (300 x 300 DPI)

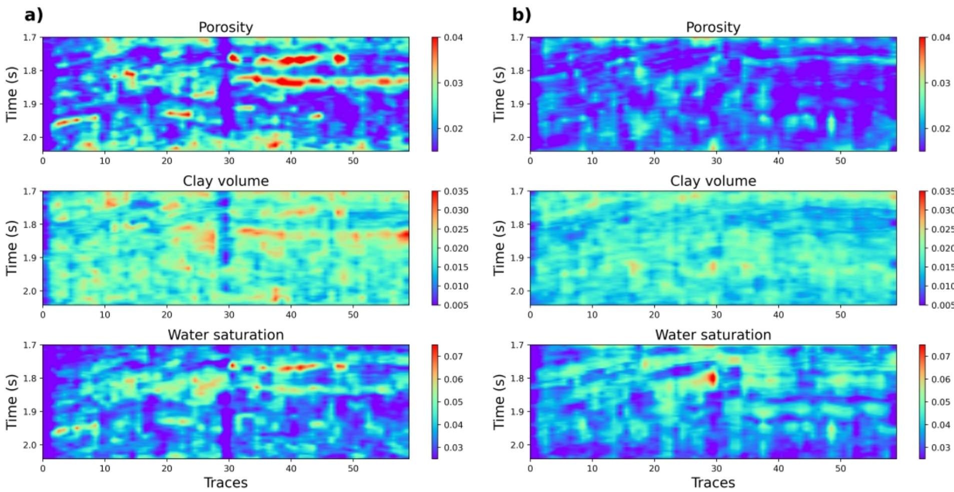

Figure 26: Uncertainty of inversion results for the real case application: a) standard deviations from regular NN, and b) standard deviations from P-PINN.

406x203mm (300 x 300 DPI)

DATA AND MATERIALS AVAILABILITY

Data associated with this research are available and can be obtained by#xD;#xA;contacting the corresponding author.

DOI:10.1190/geo2023-0214.1